PAPER

Check for updates

Effects of side reactions on the kinetics of nanoporous gold formation revealed by real-time X-ray scattering during electrolytic dealloying†

Samuel S. Welborn, [ab] John S. Corsi, [ab] Lin Wang, [a] Asaph Lee, [ac] Jintao Fu [a] and Eric Detsi *[ab]

Nanoporous gold (NP-Au) is used in various energy applications. However, little attention has been paid to the nature of surface films which can grow *via* side reactions during the formation of NP-Au by selective leaching. These films could significantly impact both the kinetics of NP-Au formation by selective leaching, and the performance of this NP-Au in specific energy applications. While it has been reported that complete removal of Ag from a Au–Ag parent alloy by selective leaching is kinetically more sluggish in $HClO_4$ than in HNO_3, and that the resulting structure size of NP-Au is smaller when formed in $HClO_4$ compared to HNO_3, these findings were not attributed to the growth of surface film *via* side reactions during selective leaching. In this work, small-angle and wide-angle X-ray scattering (SAXS and WAXS) are used in real time during NP-Au formation by selective electrolytic leaching of Ag from a Au–Ag parent alloy in 1 M $HClO_4$ and 1 M HNO_3 to demonstrate that the sluggish dealloying behavior in $HClO_4$ results from the growth of a surface film during dealloying. In $HClO_4$, Ag^+ ions released from the Au–Ag working electrode spontaneously react with Cl^- ions released from ClO_4^- reduction at the counter electrode to form an insoluble AgCl passive film on NP-Au. The AgCl hinders Ag dissolution and surface diffusion of Au atoms, slowing down the reaction kinetics and the rate of ligament growth. Our findings shed light on dealloying reaction mechanisms and will contribute to better control of the morphology and surface chemical state of nanoporous metals for energy applications.

Introduction

In the past decades, nanoporous metals have been the subject of intense research, partly owing to their wide range of potential energy applications as heterogeneous (electro)catalysts,[1–3] battery electrodes,[4,5] supercapacitors,[6,7] 3D current collectors,[8] 3D nanocapacitors,[9] and plasmonic materials.[10–12] Nanoporous metals are typically created by selectively removing a sacrificial element from a parent alloy using a variety of methods including free corrosion dealloying,[13] electrolytic dealloying,[14–16] liquid metal dealloying,[17] vapor phase dealloying,[18,19] galvanic replacement,[20] reduction-induced decomposition,[21,22] and thermal decomposition.[18,23] Nanoporous gold (NP-Au), made by selectively etching Ag from a Au–Ag parent alloy using free corrosion[13] or electrolytic[14,15] dealloying, is the most commonly

studied nanoporous metal system. Despite its success in various energy applications, however, the effects of side reactions on both the kinetics of NP-Au formation by electrolytic dealloying, and its resulting morphology are not well-understood.[14,15,24] It is well-established that during electrochemical processes the electrolyte and the electrode may undergo irreversible decompositions through side reactions, which can result in the deposition of solid products in the form of a surface film with thickness ranging from a few molecular layers up to a few nanometers at the electrode/electrolyte interface.[25,26] While many efforts under the umbrella of battery research focus on understanding and controlling these surface films to prevent material loss and stabilize the electrode material (*i.e.* the solid electrolyte interphase—SEI—layer in lithium-ion and sodium-ion batteries),[25,26] less attention has been paid to the impact of passive surface films on aqueous electrochemical systems outside of the battery community. For instance, in the case of nanoporous metal formation by dealloying, only a handful of works by Weissmüller and co-workers,[14] de Hosson and co-workers,[24] and Erlebacher and co-workers[15] suggest the formation of a solid passive film on the ligaments of NP-Au during dealloying. Understanding the nature of such a passive film, and the conditions under which this film forms during electrolytic dealloying, is critical to determining its impact on both

ᵃDepartment of Materials Science & Engineering, University of Pennsylvania, Philadelphia, PA 19104-6272, USA. E-mail: detsi@seas.upenn.edu

ᵇVagelos Institute for Energy Science and Technology (VIEST), Philadelphia, PA 19104, USA

ᶜDepartment of Physics and Astronomy, University of Pennsylvania, Philadelphia, Pennsylvania 19104, USA

† Electronic supplementary information (ESI) available. See DOI: 10.1039/d1ta04822h

dealloying kinetics and the properties/performance of as-synthesized NP-Au in energy applications. For example, a passive surface film created on NP-Au during dealloying may affect its porosity development mechanism by cutting off pathways for surface diffusion, thereby limiting ligament coarsening, and ultimately resulting in a smaller structure size.[27] When tested for its catalytic activity after dealloying, for example, the performance of this surface passivated NP-Au could yield different results compared to pure, non-passivated NP-Au. Considering that the formation of such a passive surface film directly depends on the nature of the electrolyte and the electrode used in an electrochemical process, to better serve the nanoporous metals community we performed a broad literature search to identify the type of electrolytes widely used in the field to fabricate NP-Au from Au–Ag alloys. As shown in the table and corresponding pie chart in Fig. 1, we found that perchloric acid ($HClO_4$) and nitric acid (HNO_3) are the most used electrolytes for electrolytic dealloying. Interestingly, Weissmüller and co-workers carried out a comparative study on electrolytic dealloying of NP-Au in $HClO_4$ *versus* HNO_3, and reported the following key findings (among others):[16] (i) the complete removal of Ag from the Au–Ag parent alloy is slower in $HClO_4$ compared to HNO_3; (ii) the coarsening of the ligament/pore structures during dealloying is more severe in HNO_3 than in $HClO_4$. In the present study, we hypothesized that the phenomena in (i) and (ii) are associated with the nature of the passive surface film formed with respect to the electrolyte. Thus, this article describes novel fundamental research aimed at identifying and understanding the conditions under which a passive surface film arises *via* side reactions during NP-Au formation by electrolytic dealloying in $HClO_4$, the most used electrolyte for selective electrolytic leaching of Au–Ag alloys. In this work, we aim to shed light on passive surface films, which could drastically impact the performance of NP-Au in its various energy applications.

Experimental

In situ dealloying

We used a custom Kapton pouch cell containing three electrodes and 2 mL of electrolyte to dealloy the parent Au–Ag alloy. A 5 μm-thick Au–Ag parent alloy (Custom Order, Imtradex Corp.) with composition $Au_{35}Ag_{65}$ (at%) was used as the working electrode, an Ag/AgCl in 1 M KCl was used as the reference electrode, and Pt foil was used as the counter electrode. The masses of the parent alloys for $HClO_4$ dealloying and HNO_3 dealloying were 7.2 mg and 5.2 mg, respectively. The pouch cell was mounted to a sample stage in the environmental chamber at the Dual-Source and Environmental X-ray Scattering Facility at Penn and filled with either 1 M $HClO_4$ or 1 M HNO_3, depending on the experiment. The environmental chamber was left at atmospheric pressure to avoid electrolyte evaporation. A BioLogic VMP-300 potentiostat was used to apply an oxidizing potential of 950 mV between the Au–Ag parent alloy and the Ag/AgCl reference electrode. The microstructural and crystallographic evolution was probed by aiming the Cu K_{α} beam at the Au–Ag parent alloy and detecting the scattered waves as Ag was

oxidized. Microstructural data was gathered on a small-angle 1 M pixel Pilatus detector down an evacuated flight path, and crystallographic data was gathered on a 100 K pixel Pilatus wide-angle detector in the environmental chamber nearby the sample. Each acquisition was 180 seconds. After dealloying, the sample was washed in DI water several times to remove residual electrolyte and dried in air. We used 17 M liquid ammonia in water to remove AgCl from the $HClO_4$-dealloyed sample.

SAXS fitting

Each SAXS dataset was fit using the Teubner–Strey model, which captures the characteristic spacing d in bicontinuous materials.[55,56]

Ex situ dealloying

Samples were dealloyed in the same electrolyte concentration (1 M HNO_3 and 1 M $HClO_4$) and at the same potential (950 mV) as the *in situ* experiments discussed above, this time with 10× volume of electrolyte (20 mL). The Hg/Hg_2SO_4 (in K_2SO_4, sat.) control experiment was performed in 2 mL of 1 M $HClO_4$ at potential of 530 mV under nitrogen purge to suppress the oxygen reduction reaction (ORR, see eqn (4) under Elucidation of the reaction mechanisms).

Characterization

Scanning electron microscopy (SEM, JEOL 7500F) and energy dispersive X-ray spectroscopy (EDX, EDAX Octane Elect Super) were used to investigate the microstructure and elemental composition of the *in situ* dealloyed samples. *Ex situ* XRD patterns were collected using a Rigaku MiniFlex powder diffractometer with Cu K_{α} radiation. X-ray photoelectron spectroscopy (XPS) analysis was performed using PHI Versa Probe I instrument using a 200 μm 50 W beam for acquisition. A pass energy (PE) of 23 eV for high resolution spectra windows, and PE of 117 eV was used for the survey analysis. Dual source (electron and ion gun) charge compensation was used during analysis to compensate for the shifts in the BE of the spectra. The adventitious C 1s C–C peak at 285.0 eV was used to calibrate binding energy positions.

Results and discussion

(1) Overview

As mentioned in the Introduction, during dealloying, the formation of a passive film at the electrode/electrolyte interface can impact the kinetics of the dealloying process and the morphology (*e.g.*, microstructural size and crystal structure) of the dealloyed material. The nature of this passive film directly depends on both the electrolyte and the electrode, and $HClO_4$ and HNO_3 are the most widely used electrolytes during electrolytic dealloying of Au–Ag parent alloys based on our broad literature survey in Fig. 1. In the case of $HClO_4$, we hypothesized that the Au–Ag parent alloy and the $HClO_4$ electrolyte may decompose and form insoluble compounds (*e.g.*, silver chloride—AgCl), which may deposit on the surface of the NP-Au as a passive film and hinder the dealloying rate. In the case of

This journal is © The Royal Society of Chemistry 2021

J. Mater. Chem. A, 2021, **9**, 19994–20005 | **19995**

(a)

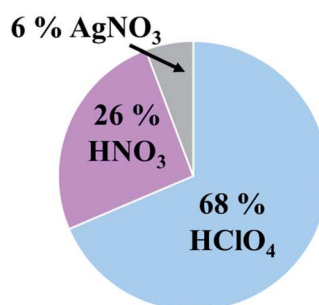| Electrolyte	Molarity (M)	Reference electrode	Applied voltage *vs.* RE (mV)	Reference
AgNO$_3$	0.1	NHE	1440–2000	[15]
	1	Ag	500	[28]
HClO$_4$	1	Ag/AgCl	600–850	[29]
	1	Ag/AgCl	700	[30]
	1	Ag/AgCl	750	[31]
	1	Ag/AgCl	750	[32]
	1	Ag/AgCl	750	[33]
	1	Ag/AgCl	750	[34]
	1	Ag/AgCl	750–850	[35]
	1	Ag/AgCl	850	[14]
	1	Ag/AgCl	850	[31]
	1	Ag/AgCl	850	[14]
	0.7–0.8	Ag/AgCl	900–1000	[36]
	1	Ag/AgCl	1000	[30]
	1	Ag/AgCl	1050	[16]
	0.7	Ag/AgCl	0–1300	[37]
	1	Ag/AgCl	1050–1200	[38]
	0.77	MSE	920–1100	[39]
	0.5	MSE	550	[40]
	0.5	MSE	300	[41]
	1	SCE	1100	[42]
	1	SCE	1038	[43]
	1	SCE	1070	[44]
	1	SCE	1040	[45]
	1	SCE	1100	[46]
	1	SCE	1000	[47]
HNO$_3$	5	Pt	60	[2]
	0.1	SCE	1100	[48]
	1	Ag	600	[49]
	5	Pt	60–300	[50]
	1	NHE	1175	[51]
	Dilute	Ag/AgCl	1300	[52]
	5	Pt	60	[53]
	5	Pt	60	[16]
	5	Pt	60	[54]

(b)

6 % AgNO$_3$

26 % HNO$_3$

68 % HClO$_4$

Fig. 1   (a) Survey of reports on NP-Au synthesized by electrolytic dealloying of Au–Ag parent alloys. Various electrolytes, molarities, reference electrodes, and applied anodic voltages are shown. Of the three electrolytes, HClO$_4$ is most widely used to synthesize NP-Au by electrolytic dealloying, followed by HNO$_3$. (b) Pie chart indicating the percentage of reports found in our survey which use HNO$_3$, HClO$_4$, and AgNO$_3$ as the electrolytic dealloying electrolyte.

HNO_3, the Au–Ag parent alloy and the HNO_3 electrolyte may also decompose, but form products that are soluble in acid or form a non-blocking film (*e.g.*, silver nitrate – $AgNO_3$, or non-dense silver oxides – AgO_x), which may not hinder the dealloying process in acids. To test our hypothesis, in the second part of the Results and discussion section, we probe the evolution of the characteristic microstructural size (using SAXS) and crystallography (using WAXS) simultaneously during electrolytic dealloying in 1 M $HClO_4$ and 1 M HNO_3. This is, to the best of our knowledge, the first time SAXS and WAXS have been used simultaneously to characterize the electrolytic dealloying of Au–Ag. In the third part of the Results and discussion section, we use new insights gained from the SAXS and WAXS data to elucidate the electrochemical reaction mechanisms occurring during NP-Au formation by electrolytic dealloying in $HClO_4$ and HNO_3, and the effects of the electrolyte on the dealloying process. In the fourth part of the Results and discussion section we elucidate the mechanism through which AgCl forms. We also propose a mechanism for Ag and Au mobility (*i.e.*, Ag atom dissolution and surface diffusion of Au atoms) during electrolytic dealloying in the presence of a passive AgCl film, building on a recent model proposed by Snyder *et al.* on electrolytic dealloying in neutral pH in the presence of a passive silver oxide film.[15] Finally, in the fifth and last part of the Results and discussion section, we clarify how the presence of a passive AgCl film can impact the performance of nanoporous gold in specific energy applications.

(2) Small- and wide-angle X-ray scattering (SAXS and WAXS)

In situ **SAXS and WAXS during electrolytic dealloying.** SAXS and WAXS were used simultaneously and in real time to study the effects of $HClO_4$ and HNO_3 on the dealloying process. Combining these techniques, we investigated the temporal evolution of both the microstructure and the crystal structure of a 5 μm-thick Au–Ag parent alloy with composition $Au_{35}Ag_{65}$ at% as Ag was removed from it electrolytically. The electrolytic

dealloying setup consists of an open-air Kapton pouch cell (see Fig. S1 in the ESI†) containing the 5 μm-thick $Au_{35}Ag_{65}$ parent alloy used as the working electrode, a platinum (Pt) foil used as the counter electrode, a Ag/AgCl reference electrode, and 2 mL of either 1 M $HClO_4$ or 1 M HNO_3 used as the electrolyte (Fig. S1†). This electrolytic cell was mounted in the chamber of a Xenocs Xeuss 2.0 scattering instrument with the X-ray chamber at atmospheric pressure and ambient temperature in air. A constant voltage of 950 mV was applied between the Au–Ag working and Ag/AgCl reference electrodes to drive the dissolution of Ag. During electrolytic dealloying, X-rays generated using a copper K_α source (Fig. S2a†) are monochromated and collimated (Fig. S2b†), and impinge on the $Au_{35}Ag_{65}$ working electrode (Fig. S2c†), interacting with it by transmission, absorption, or scattering. We found that the $Au_{35}Ag_{65}$ working electrode thickness used in our experiments (5 μm) balances these interactions to provide enough scattering intensity within our time resolution (180 seconds). The scattered waves are collected with two detectors: a small-angle detector at the end of an evacuated flight path for SAXS (Fig. S2d†), and a wide-angle detector in the environmental chamber near the sample (Fig. S2e†) for WAXS. In Fig. S2f and g,† we explored two different electrolytic dealloying cell configurations: (i) a side-by-side configuration (Fig. S2f†), where the working electrode (checkered film connected to the red line) and counter electrode (grey film connected to the blue line) sat side-by-side to avoid the interaction of the incident X-rays with the Pt foil electrode, which would otherwise weaken the intensity of the scattered X-rays collected in Fig. S2d and e.† (ii) A stacked configuration (Fig. S2g†), in which the working and counter electrodes face each other and are separated by a glass microfiber battery separator (Whatman, Grade GF/F) to prevent electrical shorting. Note that while this stacked configuration is ideal for electrochemical experiments because mass transport is optimal when the working and counter electrodes face each other, incident X-rays interacting with the Pt counter electrode weakens the intensity of the scattered X-rays collected in
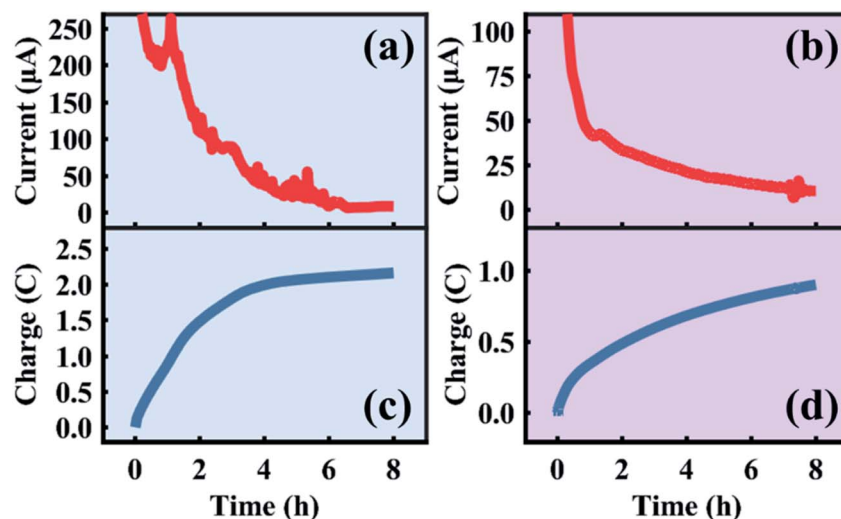

Fig. 2 Current and charge transferred during the first eight hours of the *in situ* sample dealloyed in $HClO_4$ (a and c) and HNO_3 (b and d).

This journal is © The Royal Society of Chemistry 2021

J. Mater. Chem. A, 2021, **9**, 19994–20005 | **19997**

Fig. S2d and e.† Therefore, after performing *ex situ* experiments to ensure that electrolytic dealloying proceeds similarly in the two cell configurations in Fig. S2f and g (see ESI Video 1 and Fig. S3† for *ex situ* dealloying using the stacked configuration in Fig. S2g†), we use the side-by-side configuration (Fig. S2f†) for subsequent experiments. A detailed diagram of this setup is found in Fig. S1.†

The *in situ* electrolytic dealloying data obtained are shown in Fig. 2 with background colors corresponding to the electrolyte: blue for $HClO_4$, and purple for HNO_3 (similar background colors are also used in Fig. 3–6, and S3–S8†). The current *vs.* time plots in Fig. 2a and b represent the typical electrolytic dealloying currents measured between the $Au_{35}Ag_{65}$ working electrode and the Pt counter electrode when a constant voltage of 950 mV is applied between the working and the Ag/AgCl reference electrode in 1 M $HClO_4$ electrolyte (Fig. 2a) and 1 M HNO_3 electrolyte (Fig. 2b). In Fig. 2a, there is a fluctuation in current around the end of the first hour of dealloying, which has been known to occur during electrolytic dealloying experiments when the dissolution of the sacrificial element (in our case Ag) does not occur uniformly. Typically, during dealloying, if the Ag dissolution front at the bulk electrode/electrolyte interface propagates uniformly (*i.e.*, layer-by-layer) inside the material, the dealloying current measured across the cell (*i.e.*, the Ag dissolution current) will be constant without fluctuation. In practice, however, Ag dissolution does not occur layer-by-layer: in addition to Ag removed from the bulk electrode/electrolyte interface, the electrolyte can also penetrate into the bulk of the material through cracks and grain boundaries to remove more Ag. This will cause the dealloying current to suddenly increase/fluctuate as shown Fig. 2a. Similar fluctuations have been observed in our previous work on electrolytic dealloying.[57] The corresponding plots of the cumulative charge as a function of time, associated with the amount of Ag removed during the dealloying process, are shown in Fig. 2c and d for $HClO_4$ and HNO_3, respectively. Note that in our pouch cell configuration,

the AuAg parent alloy is partially submerged into solution, and a portion of the AuAg alloy remains outside of the electrolyte to connect with the lead wire (see Fig. S2†). The magnitude of current in Fig. 2a and b is therefore associated with the active mass. We should emphasize that a difference in current magnitude does not impact our SAXS and WAXS results below as the same oxidizing potential was used (950 mV *vs.* Ag/AgCl) and porosity development was observed in both cases.

Time-resolved SAXS and WAXS collected *in situ* during Ag removal from the $Au_{35}Ag_{65}$ parent alloy are shown in Fig. 3a and b for $HClO_4$ and Fig. 3c and d for HNO_3. Time in these datasets is indicated by color, beginning in purple and ending in red. The black curve in Fig. 3b and d is the pattern of the starting $Au_{35}Ag_{65}$ parent alloy. Fig. 3e shows the average ligament–ligament distance, d, for the sample dealloyed in $HClO_4$ (squares) and in HNO_3 (circles) deduced from the SAXS data from Fig. 3b and d.[55,56] Note that in Fig. 3e, the bump marked by an asterisk for the sample dealloyed in $HClO_4$ is an experimental artifact as it has not been observed in other *d versus* time curves as shown in Fig. S4 in the ESI.†

Evolution of the crystal structure from WAXS data. To elucidate the effect of the two electrolytes on the electrolytic dealloying process, we begin by noting the striking difference between the WAXS patterns for the samples dealloyed in $HClO_4$ (Fig. 3a) and HNO_3 (Fig. 3c). On the one hand, the WAXS patterns for electrolytic dealloying in HNO_3 (Fig. 3c) show the (111) peak associated with the face-centered cubic (FCC) crystal structure of the starting $Au_{35}Ag_{65}$ evolving to NP-Au. No new peaks were observed during dealloying. A video showing the evolution of this peak in real time is provided in the ESI (ESI Video 2†). On the other hand, the WAXS patterns for electrolytic dealloying in $HClO_4$ (Fig. 3a) also shows the (111) peak for the Au–Ag solid solution evolving to NP-Au, but during the process two new peaks appear at the 2θ values of 27.8 and 32.3 as indicated by the asterisks in Fig. 3a. These peaks are attributed to AgCl (111) and (200), respectively. A close look at the time-
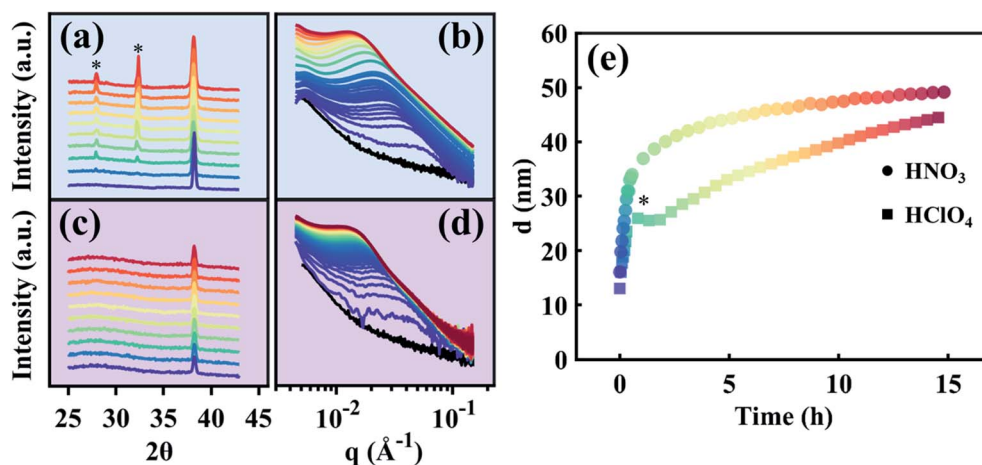

Fig. 3 Time-resolved data. Comparative view of SAXS and WAXS data during the electrolytic dealloying of a parent Au–Ag alloy into NP-Au using $HClO_4$ (a and b), and HNO_3 (c and d). In the WAXS data for the *in situ* $HClO_4$ cell (a), two peaks appear which correspond to AgCl, represented by asterisks. No such peaks arise during electrolytic dealloying in HNO_3 (c). (e) The ligament–ligament distance d of the NP-Au growing in each of the two electrolytes. HNO_3 grows rapidly at first and eventually reaches a regime of slow growth/stability, where $HClO_4$ grows at a similar pace at first, but is slowed after reaching ~25 nm.
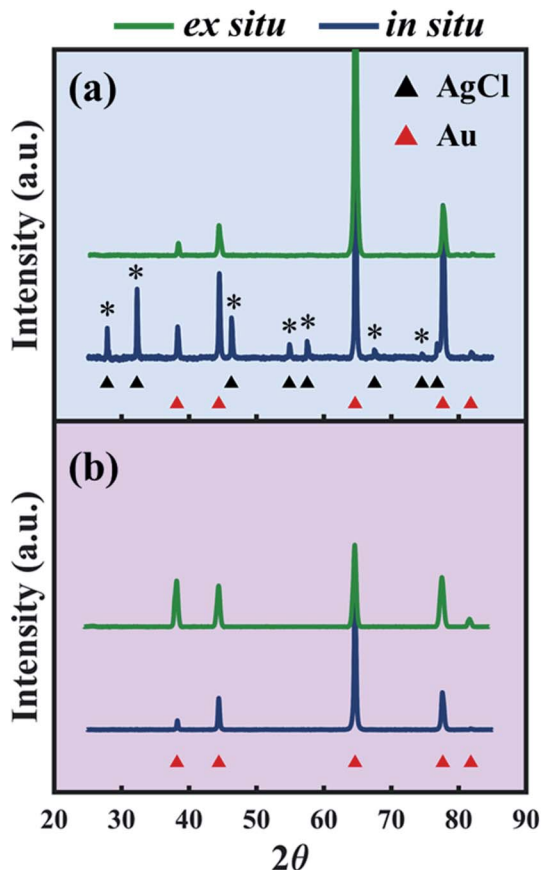
Fig. 4 (a) XRD patterns after dealloying in 1 M $HClO_4$ in small volumes (*in situ*, blue) and in large volumes (*ex situ*, green). Asterisks mark the AgCl peaks (PDF # 31-1238) formed during *in situ* dealloying. (b) XRD patterns after dealloying in 1 M HNO_3 in small volumes (*in situ*, blue) and in large volumes (*ex situ*, green).

evolution of these AgCl peaks reveals that they are not present at the beginning of the dealloying process. Instead, they appear after 1 h and gradually increase in intensity during electrolytic dealloying. A video showing the evolution of these peaks in real time can be found in the ESI (ESI Video 3†).

***Ex situ* X-ray diffraction (XRD) after electrolytic dealloying.** To confirm that AgCl formed on NP-Au during dealloying, the NP-Au dealloyed in the X-ray scattering instrument was rinsed in deionized (DI) water (note that AgCl is insoluble in DI water) and further characterized *ex situ* by XRD. The presence of AgCl was confirmed as shown by the blue pattern in Fig. 4a, where it is seen that the diffraction peaks of AgCl marked by the asterisks match with the black triangle pattern associated with AgCl (PDF # 31-1238). Furthermore, the relatively strong AgCl peak intensity indicates that it is a non-negligible component in the system. On the other hand, the *ex situ* XRD of the sample dealloyed in HNO_3 contains peaks solely from Au (PDF # 4-784) as shown by the blue curve in Fig. 4b.

Structure size evolution from SAXS data. While not immediately noticeable from the SAXS patterns in Fig. 3b and d, the microstructure of each of these systems evolves differently in time as indicated by the variation of d with time shown in

Fig. 3e. To reiterate, d is the characteristic wavelength in the system, a variable closely related to the peak position in inverse space (q) observed in the scattering patterns in Fig. 3b and d, and is roughly double the ligament size. We have employed the Gaussian Random Field (GRF)[56,58,59] model to provide representative real-space nanoporous structures at different stages of the dealloying process (Fig. S5 in the ESI†). Here, we extract real values of d from the dealloying process in $HClO_4$ and HNO_3 from Fig. 3e and plug them into the GRF model to visualize how the microstructure changes as a function of dealloying time in each case. When dealloying in HNO_3, d increases rapidly from an initial value of 16 nm (corresponding to an average ligament size of ~8 nm) to 40 nm (corresponding to a ligament size of ~20 nm) within the first 2 h (circles in Fig. 3e), and eventually reaches a slower growth regime. When dealloying in $HClO_4$, d increases from a value of ~13 nm (corresponding to a ligament size of ~6.5 nm) to ~26 nm (corresponding to a ligament size of ~13 nm) within the first 2 h. The change in d for dealloying in $HClO_4$ ($\Delta d = 13$ nm) within these first two hours is nearly half that of the change in d observed for dealloying in HNO_3 ($\Delta d = 24$). These observations clearly suggest that the initial growth and coarsening of the ligament and pore structures in NP-Au during dealloying is more severe in HNO_3 than in $HClO_4$, and as a result the feature size of NP-Au is larger for the sample dealloyed in HNO_3 than the one dealloyed in $HClO_4$. These findings are in agreement with a previous report by Weissmüller and co-workers, a comparative study on electrolytic dealloying of NP-Au in $HClO_4$ *versus* HNO_3.[16] Towards the end of the experiment, the structure size (d) of the $HClO_4$-dealloyed sample nearly intersects with that of the HNO_3 sample, indicating that the coarsening process occurs over longer periods of time in $HClO_4$ compared to HNO_3. Thus, given enough time, the structural size of NP-Au dealloyed in $HClO_4$ becomes similar to NP-Au dealloyed in HNO_3 as will be shown by electron microscopy in the following section.

Characterization by electron microscopy and X-ray photoelectron spectroscopy. Scanning electron microscopy (SEM) was used to further investigate the morphology of each of the two samples dealloyed in $HClO_4$ and HNO_3 in real time during X-ray scattering (*i.e.*, from Fig. 2 and 3). Typical SEM images of the cross sections are shown at low and high magnifications in Fig. 5. For the $HClO_4$-dealloyed sample (Fig. 5a and b), we noticed a thick and dense film on top of dealloyed NP-Au at low magnification (Fig. 5a). The expected NP-Au morphology can be observed at high magnification (Fig. 5b). Further analysis by EDX elemental mapping (see Fig. S6†) indicates that the bulk of NP-Au mostly contains Au with small amounts of Ag and Cl, while the thick film on top of NP-Au only contains Ag and Cl. This is in good agreement with the presence of AgCl detected from the WAXS and XRD data of the $HClO_4$-dealloyed sample. Considering the insolubility of AgCl in water, the $HClO_4$-dealloyed sample was washed in concentrated liquid ammonia (17 M NH_3) which is known to dissolve silver halides.[60] The thick AgCl is removed when the sample is washed in 17 M NH_3, as shown in Fig. 5e and f, and further Fig. S6 in the ESI.† In contrast to the $HClO_4$-dealloyed sample (Fig. 5a and b), the sample dealloyed in HNO_3 does not have any surface film as
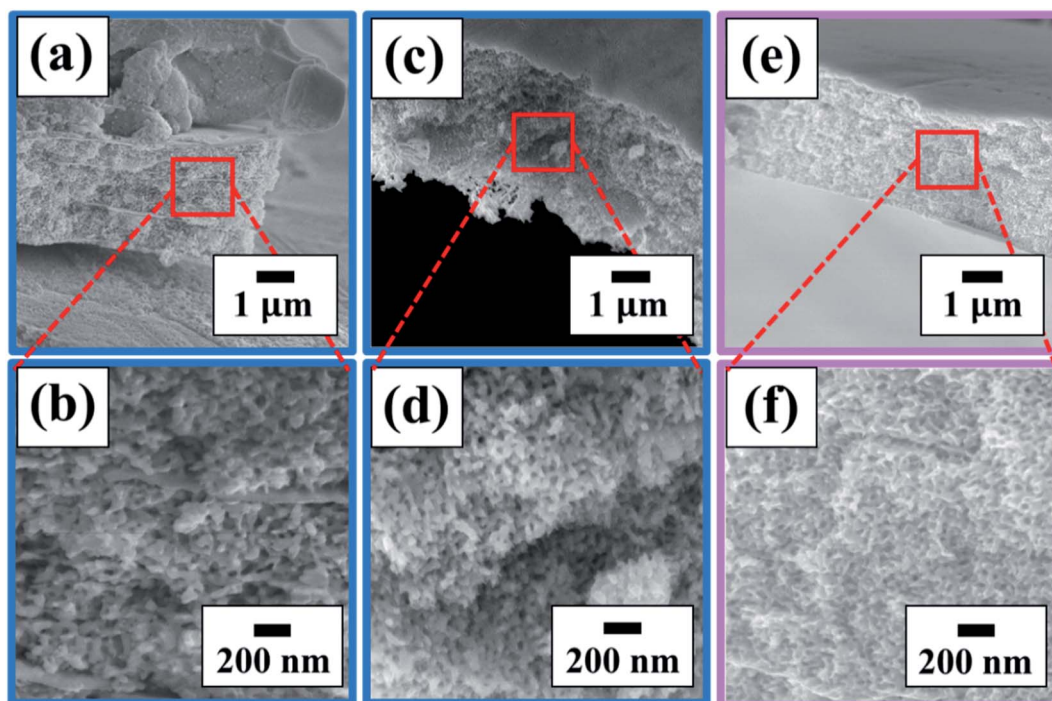
Fig. 5 SEM images of *in situ* dealloyed NP-Au. (a and b) NP-Au dealloyed in HClO$_4$, with large AgCl particles on the top surface of the film. (c and d) NP-Au dealloyed in HClO$_4$ and washed in 17 M NH$_3$ to remove residual AgCl particles. (e and f) NP-Au dealloyed in HNO$_3$.

shown in Fig. 5c and d. It should be emphasized that the presence of a small amount of Ag and Cl in the bulk of NP-Au dealloyed in HClO$_4$ as mentioned above suggests that the AgCl film may also be present on the ligaments of NP-Au as will be confirmed later using XPS. The presence of such a passive AgCl film on the ligaments of NP-Au will impact the kinetics of
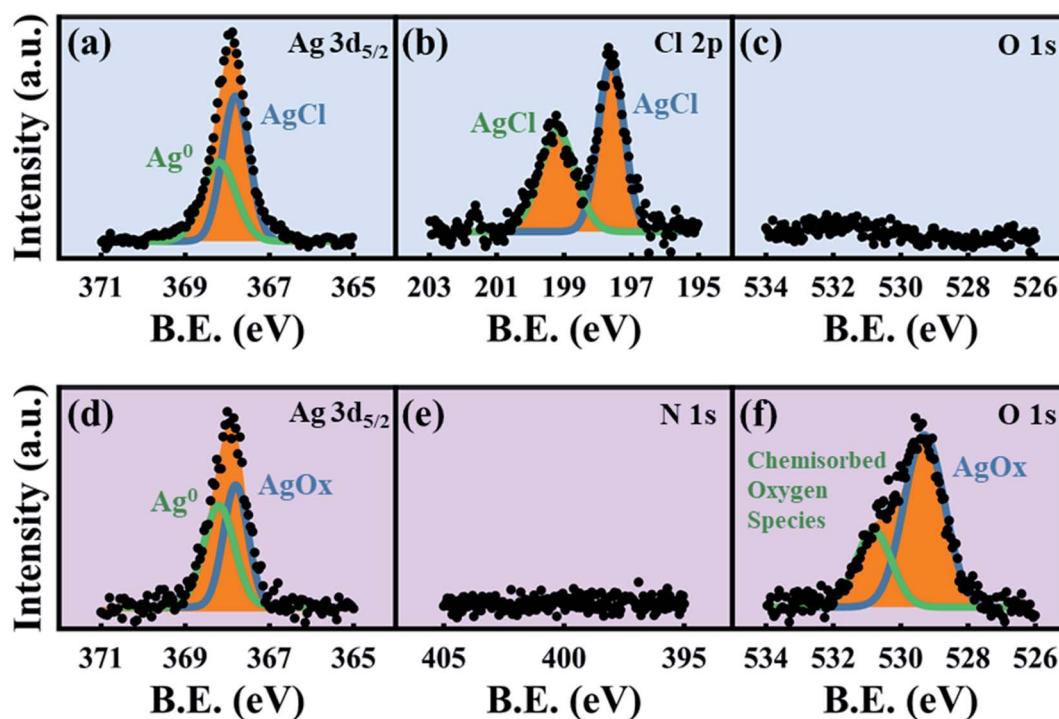

Fig. 6 XPS spectra. Top row is for the HClO$_4$-dealloyed *ex situ* sample: (a) Ag 3d$_{5/2}$, (b) Cl 2p and (c) O 1s, demonstrating AgCl growth even in larger electrolyte volumes. Bottom row is for the HNO$_3$-dealloyed *ex situ* sample: (d) Ag 3d$_{5/2}$, (e) N 1s and (f) O 1s, demonstrating that there is no nitrogen-containing surface coating.

20000 | *J. Mater. Chem. A*, 2021, **9**, 19994–20005

This journal is © The Royal Society of Chemistry 2021

the dealloying process and the growth and coarsening of these ligaments, which may explain our earlier observation (from the SAXS data) that during dealloying, the ligaments and pores are larger for the NP-Au dealloyed in HNO_3 than the one dealloyed in $HClO_4$. This aspect will be discussed at length in a later section of this work. For now, since both WAXS, XRD, SEM, and EDX mapping confirm the presence of a thick AgCl film on the NP-Au dealloyed in $HClO_4$, the straightforward question that arises is why such film has not been detected and reported earlier, considering that 1 M $HClO_4$ is the most used electrolyte for electrolytic dealloying as shown in Fig. 1. To answer this question, we must stress that a relatively large volume (several tens of mL) of 1 M $HClO_4$ is commonly used during electrolytic dealloying, whereas only ~2 mL of 1 M $HClO_4$ was used in our electrolytic cell during *in situ* dealloying. In such a small volume, the sacrificial Ag that is removed from the Au–Ag parent alloy would impart a significantly higher Ag^+ ion concentration to the electrolyte compared to larger volumes. This would lead to an increase in AgCl precipitation. To verify this hypothesis, we carried out *ex situ* dealloying for both $HClO_4$ and HNO_3, this time in 20 mL of electrolyte (a 10-fold increase in electrolyte volume), and used both XRD (Fig. 4) and XPS (Fig. 6) to characterize these films after dealloying. The only peaks identified in the *ex situ* XRD patterns for the samples dealloyed in $HClO_4$ (green line in Fig. 4a) and HNO_3 (green line in Fig. 4b) are for Au. If a very thin film of AgCl was present on the NP-Au (unlike the dense film observed from our *in situ* tests in small electrolyte volumes), it may not be detected by XRD, a bulk technique which does not have significant surface sensitivity. We believe this is the reason that, although $HClO_4$ is the most widely used electrolyte for electrolytic dealloying, the presence of AgCl on the dealloyed NP-Au has not been reported prior to the present work.

While previous reports have used XPS to analyze the surface states of dealloyed NP-Au, these studies focus mostly on elemental Ag, Au, and O,[38,61,62] and not on the electrolyte species. XPS surveys of the surface of the $HClO_4$- and HNO_3-dealloyed NP-Au samples are provided in Fig. S7 in the ESI.† The corresponding high-resolution scans associated with Ag $3d_{5/2}$, Cl 2p, and O 1s are shown in Fig. 6a–c for the $HClO_4$-dealloyed NP-Au. Similarly, the high-resolution scans associated with Ag $3d_{5/2}$, N 1s, and O 1s are shown in Fig. 6d–f for the HNO_3-dealloyed NP-Au. Starting with the high resolution Ag $3d_{5/2}$ spectra, the deconvoluted peaks for the $HClO_4$-dealloyed NP-Au in Fig. 6a indicate the presence of metallic silver (Ag^0) and AgCl as illustrated by the Ag $3d_{5/2}$ peaks at 368.2 eV (green curve) and 367.8 eV (blue curve) associated with the binding energies of Ag^0 and Ag^+, respectively.[63] The deconvoluted peaks for the HNO_3-dealloyed NP-Au in Fig. 6d also indicate the presence of Ag^0 and oxidized silver species (AgO_x) as illustrated by the Ag $3d_{5/2}$ peaks at 368.2 eV (green curve) and 367.8 eV (blue curve) associated with the binding energies of Ag^0 and Ag^+, respectively.[63] This AgO_x can form during dealloying (including residual Ag_2O, which is known to dissolve in acids). Next, to further support the presence of AgCl and AgO_x, we analyzed the high-resolution scans associated with electrolyte elements, namely Cl 2p and O 1s for the $HClO_4$-dealloyed NP-Au, and N 1s and O 1s for the
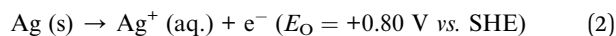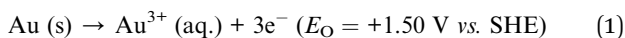
HNO_3-dealloyed NP-Au. For the $HClO_4$-dealloyed NP-Au, Fig. 6b shows two peaks in the Cl 2p scan around 197.6 eV and 199.2 eV, which match well with the binding energies of Cl $2p_{3/2}$ and Cl $2p_{1/2}$,[64,65] and can be attributed to AgCl. Further, the lack of a peak in the O 1s spectrum in Fig. 6c rules out any possibility that there is unwashed $HClO_4$ electrolyte on the sample. Thus, it can safely be concluded that even though AgCl could not be detected by XRD on NP-Au samples dealloyed *ex situ* using a relatively large volume of $HClO_4$ (green line, Fig. 4a), XPS data clearly suggest that AgCl is present on the surface of these NP-Au samples. For the HNO_3-dealloyed NP-Au sample, there is no peak in N 1s region in Fig. 6e, which is expected as nitrogen-containing species such as $AgNO_3$ are very soluble in acids. However, there is an oxygen signal (O 1s spectrum) in Fig. 6f, which can be deconvoluted into a broad peak around 529.3 eV (blue curve) ascribed to AgO_x, and a smaller peak at 530.8 eV (green curve), which is ascribed to chemisorbed oxygen.[63] Because AgCl is insoluble in most acids, the AgCl film formed during dealloying in $HClO_4$ remains on the surface of NP-Au during dealloying. This will hinder the rate of sacrificial Ag dissolution and surface diffusion of Au atoms and thus slow down the kinetics of the dealloying process and the rate of ligament growth/coarsening. Indeed, Snyder *et al.* reported that passive silver oxide films can form during electrolytic dealloying in a neutral pH electrolyte ($AgNO_3$), and proposed a mechanism for the hindrance Au and Ag mobility in their system.[15] We will return to this mechanism later in this article, and build on its insight for the present results on $HClO_4$. In contrast to $HClO_4$, since AgO_x compounds formed during dealloying in HNO_3 are soluble in acids, the rate of sacrificial Ag dissolution and the surface diffusion of Au atoms are less hindered during dealloying, and thus the kinetics of the dealloying process and the rate of ligament growth/coarsening are not hampered. The O 1s signal in Fig. 6f indicates that some of the AgO_x formed has been trapped on the pore walls during the dealloying. In order to form the passive AgCl film, there must be a source of Cl^- ions to react with the Ag^+ ions oxidized at the Au–Ag working electrode. The possibility of Cl^- originating from the Ag/AgCl reference electrode was ruled out by performing control experiments using a mercury/mercurous sulfate (Hg/Hg_2SO_4) reference electrode, which does not contain Cl^-. In other words, in our control experiments the only source of Cl^- ions is the $HClO_4$ electrolyte. Interestingly, XRD still shows that AgCl is present on the NP-Au after dealloying as shown in Fig. S8 in the ESI.†

(3) Elucidation of the reaction mechanisms

In this section, we elucidate the reaction mechanisms through which Cl^- and AgCl form during electrolytic dealloying in $HClO_4$, as well as the reaction mechanisms associated with free corrosion and electrolytic dealloying in HNO_3.
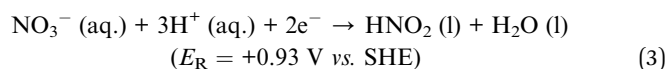
Main reactions. In general, two half-reactions take place during both free corrosion and electrolytic dealloying: (i) an oxidation half-reaction during which the sacrificial element (here Ag) is dissolved; and (ii) a reduction half-reaction during which ionic or gaseous species in the electrolyte are reduced. Starting with the oxidation half-reaction associated with the free

This journal is © The Royal Society of Chemistry 2021

J. Mater. Chem. A, 2021, **9**, 19994–20005 | **20001**

corrosion or electrolytic dealloying of a Au–Ag parent alloy, both Au and Ag are susceptible to dissolve through eqn (1) and (2), respectively, depending on strength of the corroding medium for free corrosion dealloying, and the magnitude of the applied potential for electrolytic dealloying:[66]

$$Au \text{ (s)} \rightarrow Au^{3+} \text{ (aq.)} + 3e^- \ (E_O = +1.50 \text{ V } vs. \text{ SHE}) \quad (1)$$

$$Ag \text{ (s)} \rightarrow Ag^+ \text{ (aq.)} + e^- \ (E_O = +0.80 \text{ V } vs. \text{ SHE}) \quad (2)$$

Typically, in order to oxidize Ag and leave Au behind unoxidized to create NP-Au by electrolytic dealloying, the magnitude of the voltage applied must be greater than 0.79 V vs. SHE but less than 1.52 V vs. SHE. In all of the electrolytic dealloying experiments in $HClO_4$ and HNO_3 done in the present work, the applied voltage sat between these potentials at 0.95 V vs. Ag/AgCl, which corresponds to 1.17 V vs. SHE.[66]
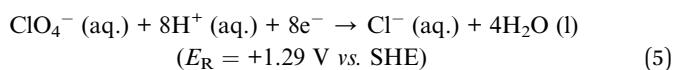
Next, we discuss the reduction half-reaction associated with free corrosion and electrolytic dealloying. In free corrosion dealloying (i.e. etching away Ag in concentrated HNO_3 without using an external bias), the counter reaction to eqn (2) is the reduction of nitrate ions, which occurs spontaneously through eqn (3) and provides sufficient potential to oxidize Ag:[66,67]

$$NO_3^- \text{ (aq.)} + 3H^+ \text{ (aq.)} + 2e^- \rightarrow HNO_2 \text{ (l)} + H_2O \text{ (l)}$$
$$(E_R = +0.93 \text{ V } vs. \text{ SHE}) \quad (3)$$

In practice, for free corrosion dealloying to occur, highly concentrated HNO_3 is necessary to overcome the high reaction overpotentials by increasing the potential of the reduction half-reaction in eqn (3).[67] For example, the potential of eqn (3) is increased from 0.93 V to 1.07 V vs. SHE if the concentration of HNO_3 is increased from 1 M to 15 M. In other words, for the present work, Ag removal from Au–Ag by free corrosion in 1 M HNO_3 through eqn (2) in combination with eqn (3) is not kinetically favorable. Instead, a bias voltage is used to electrolytically dissolve Ag through eqn (2) in combination with an appropriate reduction half-reaction. This reduction reaction takes place at the Pt counter electrode during electrolytic dealloying. To our knowledge, the nature of the counter half-reaction has not been reported and needs to be identified. For electrolytic dealloying in $HClO_4$ we identify three candidates for reduction at the Pt counter electrode. The first is O_2, which in acidic solution can be reduced in the ORR in eqn (4):

$$O_2 \text{ (g)} + 4H^+ \text{ (aq.)} + 4e^- \rightarrow 2H_2O \text{ (l)} \ (E_R = +1.23 \text{ V } vs. \text{ SHE}) \quad (4)$$
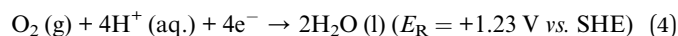
The second is ClO_4^-, which can decompose into Cl^- ions through eqn (5):[68]

$$ClO_4^- \text{ (aq.)} + 8H^+ \text{ (aq.)} + 8e^- \rightarrow Cl^- \text{ (aq.)} + 4H_2O \text{ (l)}$$
$$(E_R = +1.29 \text{ V } vs. \text{ SHE}) \quad (5)$$

And finally, Ag plating is possible based on eqn (6):

$$Ag^+ \text{ (aq.)} + e^- \rightarrow Ag \text{ (s)}, (E_R = +0.80 \text{ V } vs. \text{ SHE}) \quad (6)$$
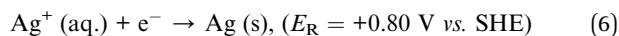
Thermodynamically, when there are many possible reduction half-reactions, the one with the highest reduction potential proceeds first (i.e., the ClO_4^- reduction reaction in eqn (5)). However, if the reaction kinetics are sluggish, a reduction half-reaction with lower reduction potentials may proceed first. Out of the three possible counter reactions in eqn (4)–(6), the kinetics of the Ag^+ deposition onto the counter electrode through eqn (6) is expected to be very favorable, but this reaction cannot occur before Ag^+ ions are sufficiently present in solution. Thus, the only possible reactions in the early stages of dealloying are ORR (eqn (4)) and ClO_4^- reduction (eqn (5)). In practice, eqn (4) and (5) are kinetically sluggish but Pt catalyzes both of these reactions and thereby reduces their overpotentials.[68,69] It is well-known in the electrocatalysis community that for the ORR reaction in eqn (4) to proceed continuously, the electrolyte to should be saturated with O_2 gas, which is not the case during our electrolytic dealloying process. Therefore, we point to the reaction in eqn (5) as the main counter half-reaction during electrolytic dealloying in $HClO_4$ in combination with eqn (2). At a later stage of the dealloying process (when the concentration of Ag^+ in the electrolyte is high enough), the half-reaction in eqn (6) may proceed. This can be confirmed by the presence of metallic Ag on the Pt counter electrode.

Side reactions. During electrolytic dealloying in $HClO_4$, Cl^- ions are created at the counter electrode through the reduction of ClO_4^- in eqn (5) spontaneously reacts ($\Delta G < 0$) with Ag^+ produced at the working electrode through the oxidation half-reaction in eqn (2) to form AgCl (s) through eqn (7):

$$Ag^+ + Cl^- \rightarrow AgCl \text{ (s)} (\Delta G = -55.7 \text{ kJ mol}^{-1}) \quad (7)$$
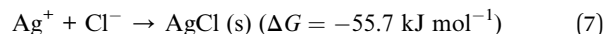
This AgCl (s) product is insoluble in water,[60] and thus remains on NP-Au. On the other hand, the counter reactions in HNO_3 do not form products that can react with Ag^+ to form a blocking film on the surface. In addition to ORR (eqn (4)) and Ag plating (eqn (6)), NO_3^- can be reduced to HNO_2 (l) in eqn (3), and gaseous products including NO_2 (g) and NO (g).[66] Ag^+ ions neither react with the electrolyte ions (NO_3^-), nor the reaction products in eqn (3), to form an insoluble blocking film, as evidenced by a lack of N species in our XPS data in Fig. 6e.

(4) Proposed mechanism of Au and Ag mobility in the presence of a passivating AgCl film

Based on the early understanding of the porosity evolution mechanism during dealloying,[13] during selective leaching of a Au–Ag parent alloy, sacrificial Ag atoms dissolve in the electrolyte while Au atoms remaining at the electrode/electrolyte interface diffuse about to form Au clusters, which further grow into coarsened ligaments (i.e. post-dealloying coarsening). This mechanism, however, assumes a "clean" electrode/electrolyte interface that only comes into contact with the electrolyte and does not contain a passivating surface film. The presence of a passivating AgCl surface film at the electrode/electrolyte interface as reported in our work will hinder the mobility of Ag and Au atoms. The first model of the porosity evolution mechanism during dealloying that takes into account
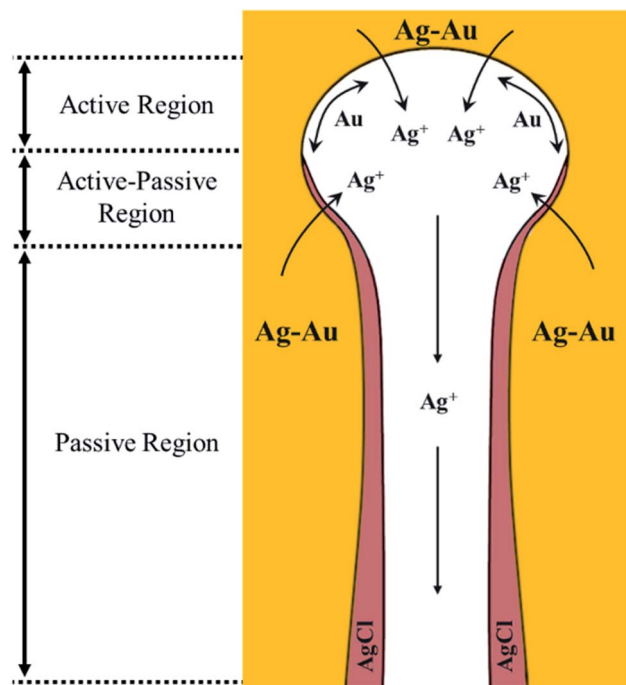
20002 | J. Mater. Chem. A, 2021, **9**, 19994–20005

This journal is © The Royal Society of Chemistry 2021

Fig. 7 Au and Ag mobility mechanism in the presence of a passivating AgCl film formed during dealloying in HClO$_4$. The three regions proposed are as follows: (1) active region: the etch front without a passive film, where Ag atoms can oxidize from the bulk Ag–Au electrode and Au is free to diffuse on the pore wall. (2) Active–passive region of competing dissolution of Ag and AgCl formation. (3) Passive region: a region where Ag oxidation from the bulk Au–Ag electrode is not possible due to a thick, passive AgCl film in the pore channel. Illustration adapted from the work of Snyder et al., DOI: 10.1149/1.2940319. Copyright The Electrochemical Society. Adapted by permission of IOP Publishing. All rights reserved.[15]

a passivating film was reported by Snyder et al.[15] Their study involved creating nanoporous Au by electrolytic removal of Ag from a Au–Ag parent alloy in a neutral pH electrolyte, an aqueous solution of AgNO$_3$, to circumvent using corrosives such as HNO$_3$ or HClO$_4$. In their work, they reported the formation of a silver oxide (Ag$_x$O) passivating film during electrolytic dealloying that hinders Ag and Au mobility and slows down the ligament coarsening significantly. The authors proposed a mechanism for Au surface diffusion and Ag dissolution in the presence of a Ag$_x$O passive film based on local pH gradients. They suggested the existence of the following three regions inside the pores.[15] Region 1: the etch front, which has a lower pH compared to the rest of the pore. This region of low pH facilitates the dissolution of Ag and surface diffusion of Au. Region 2: the intermediate region adjacent to the etch front, where the Ag$_x$O layer starts to form. Region 3: the porous channels through which removed Ag$^+$ ions diffuse and dissolve into the bulk electrolyte. Based on our results from SAXS, WAXS, SEM, EDX, XRD, and XPS, we build on the above model of Snyder et al., to explain the hindrance of Ag and Au mobility in our system, and propose the following regions within a nanopore which we graphically depict in Fig. 7 adapted from the work of Snyder et al.:[15]

Active region. Since dealloying occurs in our system, this necessitates an etch front that facilitates Ag atom dissolution and surface diffusion of Au. This corresponds to region 1 from the work of Snyder et al. We call this region the active region as in the field of corrosion science.[70] In this region, the mobility of Ag and Au is not hindered.

Active–passive region. Since a passivating AgCl film forms, there has to be a region adjacent to the etch front where this AgCl film nucleates. This corresponds to region 2 from the work of Snyder et al. More importantly, since the formation of a fully blocking AgCl film is a gradual process (i.e., it does not suddenly block Ag atom diffusion out of the bulk Au–Ag alloy), we speculate that in this second region, the formation of AgCl occurs concurrently with the corrosion of sacrificial Ag. This means that some Ag can still diffuse through the AgCl film to go into the pore channel and dissolve into the electrolyte. Thus, in this second region, there is a competition between Ag dissolution and AgCl formation similar to common passivation processes in the field of corrosion science. We call this region the active–passive region.[70] In this region, the mobility of Ag and Au is partially hindered by a relatively thin AgCl film.

Passive region. As the AgCl film grows thicker, Ag diffusion through it will become more and more difficult, to the point where the AgCl will block its diffusion into the pore channel and dissolution into the electrolyte. Thus, a fully blocking AgCl film forms. This corresponds to region 3 from the work of Snyder et al. We call this region the passive region.[70] In this region, the mobility of Ag and Au is totally hindered by a blocking AgCl film.

(5) Impact of passive film on energy applications

Various energy applications based on NP-Au can be impacted by this AgCl passive film. Two of them include the use of NP-Au as an (electro)catalyst,[2,71] and as an electrochemical actuator to convert electrochemical energy into mechanical energy.[72–77] In the former case, the remarkable (electro)catalytic performance of NP-Au made by selective removal of Ag from Au–Ag alloys is usually attributed to specific catalytic sites such as {100} facets, or to residual sacrificial Ag atoms near the surface of NP-Au.[2,71] The presence of a passive film at the surface of NP-Au will obviously prevent these active catalytic sites from coming in direct contact with the liquid or gas reactant, in order for the catalytic reaction to take place. This raises a fundamental question pertaining to the origin of the remarkable (electro) catalytic performance of dealloyed nanoporous metals. In the latter case, nanoporous metals have been reported to perform very well as electrochemical actuators,[72–77] known as metallic muscles,[78] in which the actuation mechanism takes advantage of charge-induced changes in surface stress.[72,79,80] An unexpected sign-inversion in the surface stress response of nanoporous metals has recently been reported during electrochemical actuation.[14,74] Such a sign-inversion response was associated with a passive film present at the internal surface of freshly dealloyed nanoporous metals.[14,74] Hence, passive films directly impact the performance of nanoporous metal electrochemical actuators.

Conclusion

In summary, X-ray scattering techniques (SAXS and WAXS) were used in real time during NP-Au formation by selective electrolytic removal of Ag from a Au–Ag parent alloy (dealloying) in 1 M $HClO_4$ and 1 M HNO_3 electrolytes. We studied the impacts of side reactions on the reaction kinetics and on the morphology of the fabricated NP-Au in each of these electrolytes. By combining *in situ* SAXS and WAXS data with *ex situ* XRD, SEM, EDX, and XPS data, it was found that during electrolytic dealloying in $HClO_4$, the Ag^+ ions released during Ag oxidation at the Au–Ag working electrode spontaneously react with Cl^- ions released during the reduction of ClO_4^- ions on the Pt counter electrode to form an insoluble AgCl passive film on the surface of NP-Au. We propose a mechanism for Au and Ag mobility in the presence of a passivating AgCl film formed during electrolytic dealloying in $HClO_4$, building on insights from a previous report of passive film formation during electrolytic dealloying in neutral pH. The presence of the AgCl film at the Au–Ag/$HClO_4$ interface is expected to hinder both the dissolution of Ag into the electrolyte and the surface diffusion of Au atoms left behind, which will ultimately slow down the dealloying reaction kinetics and the rate of ligament growth and coarsening. During electrolytic dealloying in HNO_3, on the other hand, it was found that AgO_x forms at the Au–Ag/HNO_3 interface. However, because AgO_x compounds are very soluble in acids, they do not form an ion-blocking passive film at the electrode/electrolyte interface even though residual AgO_x can be trapped in the pores of NP-Au during dealloying. As a result, the reaction kinetics are less hampered in HNO_3 and the ligaments grow larger during the initial stages of dealloying. These new insights should contribute to a better understanding of the reaction mechanisms in dealloying, and to a better control of the morphology and surface chemical state of dealloyed nanoporous metals for specific applications.

Conflicts of interest

There are no conflicts to declare.

Acknowledgements

References

1 T. T. H. Hoang and A. A. Gewirth, *ACS Catal.*, 2016, **6**, 1159–1164.

2 A. Wittstock, V. Zielasek, J. Biener, C. M. Friend and M. Bäumer, *Science*, 2010, **327**, 319–322.

3 Z. Wang, J. Du, Y. Zhang, J. Han, S. Huang, A. Hirata and M. Chen, *Nano Energy*, 2019, **56**, 286–293.

4 E. Detsi, X. Petrissans, Y. Yan, J. B. Cook, Z. Deng, Y.-L. Liang, B. Dunn and S. H. Tolbert, *Phys. Rev. Mater.*, 2018, **2**, 55404.

5 M. Li, Z. Wang, J. Fu, K. Ma and E. Detsi, *Scr. Mater.*, 2019, **164**, 52–56.

6 F. Meng and Y. Ding, *Adv. Mater.*, 2011, **23**, 4098–4102.

7 X. Lang, A. Hirata, T. Fujita and M. Chen, *Nat. Nanotechnol.*, 2011, **6**, 232–236.

8 J. Ye, A. C. Baumgaertel, Y. M. Wang, J. Biener and M. M. Biener, *ACS Nano*, 2015, **9**, 2194–2202.

9 S. S. Welborn, S. Van Der Meer, J. S. Corsi, J. T. M. De Hosson and E. Detsi, *ACS Appl. Mater. Interfaces*, 2021, **13**, 11721–11731.

10 E. Detsi, M. Salverda, P. R. Onck and J. T. M. De Hosson, *J. Appl. Phys.*, 2014, **115**, 44308.

11 X. Lang, L. Qian, P. Guan, J. Zi and M. Chen, *Appl. Phys. Lett.*, 2011, **98**, 93701.

12 A. Pröschel, J. Chacko, R. Whitaker, M. A. U. Chen and E. Detsi, *J. Electrochem. Soc.*, 2019, **166**, H146–H150.

13 J. Erlebacher, M. J. Aziz, A. Karma, N. Dimitrov and K. Sieradzki, *Nature*, 2001, **410**, 450–453.

14 H. J. Jin, S. Parida, D. Kramer and J. Weissmüller, *Surf. Sci.*, 2008, **602**, 3588–3594.

15 J. Snyder, K. Livi and J. Erlebacher, *J. Electrochem. Soc.*, 2008, **155**, C464.

16 M. Graf, B. Roschning and J. Weissmüller, *J. Electrochem. Soc.*, 2017, **164**, C194–C200.

17 T. Wada, K. Yubuta, A. Inoue and H. Kato, *Mater. Lett.*, 2011, **65**, 1076–1078.

18 L. Lu, P. Andela, J. T. M. De Hosson and Y. Pei, *ACS Appl. Nano Mater.*, 2018, **1**, 2206–2218.

19 M. Kosmidou, M. J. Detisch, T. L. Maxwell and T. J. Balk, *MRS Commun.*, 2019, **9**, 144–149.

20 W. Yang, X.-G. Zheng, S.-G. Wang and H.-J. Jin, *J. Electrochem. Soc.*, 2018, **165**, C492–C496.

21 Q. Chen, *J. Electrochem. Soc.*, 2014, **161**, H643–H646.

22 C. Wang and Q. Chen, *Chem. Mater.*, 2018, **30**, 3894–3900.

23 S. Chatterjee, A. Anikin, D. Ghoshal, J. L. Hart, Y. Li, S. Intikhab, D. A. Chareev, O. S. Volkova, A. N. Vasiliev, M. L. Taheri, N. Koratkar, G. Karapetrov and J. Snyder, *Acta Mater.*, 2020, **184**, 79–85.

24 E. Detsi, S. Punzhin, J. Rao, P. R. Onck and J. T. M. De Hosson, *ACS Nano*, 2012, **6**, 3734–3744.

25 H. Kumar, E. Detsi, D. P. Abraham and V. B. Shenoy, *Chem. Mater.*, 2016, **28**, 8930–8941.

26 X.-B. Cheng, R. Zhang, C.-Z. Zhao, F. Wei, J.-G. Zhang and Q. Zhang, *Adv. Sci.*, 2016, **3**, 1500213.

27 Y. C. K. Chen-Wiegart, S. Wang, Y. S. Chu, W. Liu, I. McNulty, P. W. Voorhees and D. C. Dunand, *Acta Mater.*, 2012, **60**, 4972–4981.

28 K. Ma, J. S. Corsi, J. Fu and E. Detsi, *ACS Appl. Nano Mater.*, 2018, **1**, 541–546.

29 S. Parida, D. Kramer, C. A. Volkert, H. Rösner, J. Erlebacher and J. Weissmüller, *Phys. Rev. Lett.*, 2006, **97**, 35504.

30 P. Gao, P. Qian, L. Qiao, A. A. Volinsky and Y. Su, *Scr. Mater.*, 2019, **168**, 1–4.

31 C. Lakshmanan, R. N. Viswanath, R. Rajaraman, S. Dash and A. K. Tyagi, *Mater. Today: Proc.*, 2016, **3**, 1702–1706.

32 A. K. Mishra, C. Bansal and H. Hahn, *J. Appl. Phys.*, 2008, **103**, 94308.

33 L.-H. Shao, H.-J. Jin, R. N. Viswanath and J. Weissmüller, *Europhys. Lett.*, 2010, **89**, 66001.

34 L.-Z. Liu, X.-L. Ye and H.-J. Jin, *Acta Mater.*, 2016, **118**, 77–87.

35 B. Roschning and J. Weissmüller, *Adv. Mater. Interfaces*, 2020, **7**, 2001415.

36 M. Kim, W.-J. Ha, J.-W. Anh, H.-S. Kim, S.-W. Park and D. Lee, *J. Alloys Compd.*, 2009, **484**, 28–32.

37 O. Okman and J. W. Kysar, *J. Alloys Compd.*, 2011, **509**, 6374–6381.

38 M. Graf, M. Haensch, J. Carstens, G. Wittstock and J. Weissmüller, *Nanoscale*, 2017, **9**, 17839–17848.

39 N. A. Senior and R. C. Newman, *Nanotechnology*, 2006, **17**, 2311–2316.

40 A. A. El-Zoka, B. Langelier, G. A. Botton and R. C. Newman, *Mater. Charact.*, 2017, **128**, 269–277.

41 A. F. Ebrahimy, B. Langelier and R. C. Newman, *Mater. Today Commun.*, 2020, **25**, 101371.

42 F. Liu, X.-L. Ye and H.-J. Jin, *Phys. Chem. Chem. Phys.*, 2017, **19**, 19217–19224.

43 S.-M. Zhang and H.-J. Jin, *Appl. Phys. Lett.*, 2014, **104**, 101905.

44 X.-L. Ye, N. Lu, X.-J. Li, K. Du, J. Tan and H.-J. Jin, *J. Electrochem. Soc.*, 2014, **161**, C517–C526.

45 P. Gao, X. Ye, Z. Zhu, Y. Wu, A. A. Volinsky, L. Qiao and Y. Su, *Scr. Mater.*, 2016, **119**, 51–54.

46 R. Musat, S. Moreau, F. Poidevin, M. H. Mathon, S. Pommeret and J. P. Renault, *Phys. Chem. Chem. Phys.*, 2010, **12**, 12868–12874.

47 S. G. Corcoran, *Proceedings of the Symposium on Critical Factors in Localized Corrosion III*, The Electrochemical Society, 1999, pp. 500–507.

48 M. Hakamada and M. Mabuchi, *Mater. Lett.*, 2008, **62**, 483–486.

49 A. M. Hodge, J. R. Hayes, J. A. Caro, J. Biener and A. V. Hamza, *Adv. Eng. Mater.*, 2006, **8**, 853–857.

50 A. Lackmann, M. Bäumer, G. Wittstock and A. Wittstock, *Nanoscale*, 2018, **10**, 17166–17173.

51 N. Badwe, X. Chen and K. Sieradzki, *Acta Mater.*, 2017, **129**, 251–258.

52 P. Wahl, T. Traußnig, S. Landgraf, H.-J. Jin, J. Weissmüller and R. Würschum, *J. Appl. Phys.*, 2010, **108**, 73706.

53 L. V. Moskaleva, S. Röhe, A. Wittstock, V. Zielasek, T. Klüner, K. M. Neyman and M. Bäumer, *Phys. Chem. Chem. Phys.*, 2011, **13**, 4529–4539.

54 A. Lackmann, C. Mahr, M. Schowalter, L. Fitzek, J. Weissmüller, A. Rosenauer and A. Wittstock, *J. Catal.*, 2017, **353**, 99–106.

55 M. Teubner and R. Strey, *J. Chem. Phys.*, 1987, **87**, 3195–3200.

56 S. S. Welborn and E. Detsi, *Nanoscale Horiz.*, 2020, **5**, 12–24.

57 E. Detsi, M. Van De Schootbrugge, S. Punzhin, P. R. Onck and J. T. M. De Hosson, *Scr. Mater.*, 2011, **64**, 319–322.

58 Y. Li, B.-N. Dinh Ngô, J. Markmann and J. Weissmüller, *Phys. Rev. Mater.*, 2019, **3**, 76001.

59 C. Soyarslan, S. Bargmann, M. Pradas and J. Weissmüller, *Acta Mater.*, 2018, **149**, 326–340.

60 H. Hunt and L. Boncyk, *J. Am. Chem. Soc.*, 1933, **55**, 3528–3530.

61 B. Zugic, L. Wang, C. Heine, D. N. Zakharov, B. A. J. Lechner, E. A. Stach, J. Biener, M. Salmeron, R. J. Madix and C. M. Friend, *Nat. Mater.*, 2017, **16**, 558–564.

62 S. Röhe, K. Frank, A. Schaefer, A. Wittstock, V. Zielasek, A. Rosenauer and M. Bäumer, *Surf. Sci.*, 2013, **609**, 106–112.

63 N. J. Firet, M. A. Blommaert, T. Burdyny, A. Venugopal, D. Bohra, A. Longo and W. A. Smith, *J. Mater. Chem. A*, 2019, **7**, 2597–2607.

64 J. Luo, Q. Yin, J. Zhang, S. Zhang, L. Zheng and J. Han, *ACS Appl. Energy Mater.*, 2020, **3**, 4559–4568.

65 N. Zhao, X. Fei, X. Cheng and J. Yang, *IOP Conf. Ser.: Mater. Sci. Eng.*, 2017, **242**, 12002.

66 P. Vanýsek, *Handb. Chem. Phys.*, 2012, **93**, 5–80.

67 J. Fu, Z. Deng and E. Detsi, *JOM*, 2019, **71**, 1581–1589.

68 E. T. Urbansky, *Biorem. J.*, 1998, **2**, 81–95.

69 W. Chen, J. Huang, J. Wei, D. Zhou, J. Cai, Z.-D. He and Y.-X. Chen, *Electrochem. Commun.*, 2018, **96**, 71–76.

70 J. R. Davis, *Corrosion: Understanding the Basics*, ASM International, Materials Park, OH, 2000.

71 Z. Wang, P. Liu, J. Han, C. Cheng, S. Ning, A. Hirata, T. Fujita and M. Chen, *Nat. Commun.*, 2017, **8**, 1066.

72 J. Weissmüller, R. N. Viswanath, D. Kramer, P. Zimmer, R. Würschum and H. Gleiter, *Science*, 2003, **300**, 312–315.

73 E. Detsi, P. Onck and J. T. M. De Hosson, *ACS Nano*, 2013, **7**, 4299–4306.

74 H. J. Jin, X. L. Wang, S. Parida, K. Wang, M. Seo and J. Weissmüller, *Nano Lett.*, 2010, **10**, 187–194.

75 C. Cheng and A. H. W. Ngan, *ACS Nano*, 2015, **9**, 3984–3995.

76 M. Hakamada and M. Mabuchi, *Procedia Engineering*, Elsevier B.V., 2014, vol. 81, pp. 2159–2164.

77 J. Zhang, Q. Bai and Z. Zhang, *Nanoscale*, 2016, **8**, 7287–7295.

78 R. H. Baughman, *Science*, 2003, **300**, 268–269.

79 E. Detsi, M. S. Sellès, P. R. Onck and J. T. M. De Hosson, *Scr. Mater.*, 2013, **69**, 195–198.

80 C. Stenner, L. H. Shao, N. Mameka and J. Weissmuller, *Adv. Funct. Mater.*, 2016, **26**, 5174–5181.

This journal is © The Royal Society of Chemistry 2021

J. Mater. Chem. A, 2021, **9**, 19994–20005 | **20005**